remote sensing

MDPI

Article

Phase Shift Analysis of Cryosat-2 SARin Waveforms: Inland Water Off-Pointing Corrections

Philip Moore * and Christopher Pearson

School of Engineering, Newcastle University, Newcastle NE1 7RU, UK
* Correspondence: philip.moore@ncl.ac.uk

Highlights

What are the main findings?

- SARin data can be used to derive the roll-angle from oceanic passes and the off-pointing angle of cross-track water reflectors.
- Estimation of offset-angle enables correction for GDR altimetric height and location of inland water reflectors.

What are the implications of the main findings?

- Correction for cross track reflectors yields additional height data for inland water studies.
- Even for inland water identifiable at nadir, off-pointing considerations can improve the water height estimation.

Abstract

Cryosat-2 SARin altimetric FBR data facilitates an opportunity to investigate phase differences between inland water radar reflections at the two antennae. With the antennae positioned cross-track, SARin was designed for the recovery of slope over ice margins, but here, it was used to recover off-pointing over inland waters. The ability to measure non-nadir off-pointing is verified using ocean data near the Amazon estuary to determine the satellite roll angle. Over inland waters, off-pointing requires correction to the nadir range and the geographic location of the reflectance. By using an SRTM-based water mask, the number of inland water reflectance increases significantly when off-pointing is considered. Comparisons between altimetric and river heights utilise gauge data at Tabatinga on the Solimões–Amazon. A least-squares adjustment yielded a river slope of -0.03506 ± 0.00003 m/km and a mean velocity of 1.803 ± 0.014 m/s over a river stretch of nearly 290 km. RMSE differences between the gauge and altimetry improve from 0.423 m to 0.404 m when off-pointing is taken into account for nadir inland water returns, showing the asymmetric effect of off-pointing. If all potential off-pointings are considered, the number of measurements increases by 66%, but the RMSE of 0.524 m is higher due to additional errors in the off-pointing corrections.

Keywords: altimetry; Cryosat-2; SARin; waveforms; off-nadir pointing; phase shift; Amazon hydrology

Academic Editor: Gino Dardanelli

Received: 16 August 2025
Revised: 26 October 2025
Accepted: 28 October 2025
Published: 2 November 2025

Citation: Moore, P.; Pearson, C. Phase Shift Analysis of Cryosat-2 SARin Waveforms: Inland Water Off-Pointing Corrections. *Remote Sens.* **2025**, *17*, 3627. https://doi.org/10.3390/rs17213627

1. Introduction

Satellite altimetry has a well-established capability for monitoring the height of rivers and lakes, as demonstrated in numerous publications (e.g., [1–4]) based on con-

ventional pulse-limited altimeters. More recently, SAR altimetry on board Cryosat-2 and Sentinel3/6 [5,6] is providing height data with enhanced along-track resolution for inland water studies [7–14]. With land contamination being problematic in the waveform, special approaches for retracking, including the use of sub-waveforms (e.g., [15–19]) and eliminating unreliable observations (e.g., [20]), have been proposed. Despite these efforts, estimated heights are dependent on the target characteristics, with comparison of altimetric heights against in situ gauge data giving root mean square errors (RMSEs) of up to several decimetres (e.g., [4,21]).

For all conventional pulse-limited nadir-pointing altimeters, the altimetric footprint is circular, with off-nadir radar reflections occurring near inland water bodies, as water is a better reflector than land. Along-track, this is often called the hooking effect and identified in altimetric waveforms as spikes after the nadir reflection [22,23]. In terms of altimetric range, the hooking effect can be identified by upward-pointing parabolas, as the slant range to the water reflection increases before and after the altimeter overflies the water body. If not corrected, the slant range is interpreted as the nadir range with an underestimation of the estimated water surface height. Off-pointing is particularly pertinent to narrow rivers with a limited number of altimetric heights compared with large rivers. Several studies have presented corrections for the hooking effect [22–28]. All require identification of the parabolic shape. Furthermore, all utilise conventional altimeters rather than the SAR altimeter of Cryosat-2. Indeed, Ref. [28] state that "SAR altimetry data, like Cryosat-2 data, is less prone to the hooking effect and does not require its correction." The less prone statement is true in the along-track direction, as the beam is directed to ground points, but Cryosat-2 and other satellites are affected by off-nadir reflectors cross-track. By considering the Full Bit Rate (FBR) waveform data in SARin mode, the cross-angle can be estimated, enabling identification of the water body and correction for the slant range. To distinguish from previous studies, the terminology off-pointing is used to distinguish from the hooking effect, as the causes are fundamentally different. Here, the cross-track location of the reflection is described by the cross-angle.

Cryosat-2, launched in 2010, is designed to operate in one of three modes: SAR, SARin, and the standard low-resolution mode (LRM) of earlier altimetric satellites, such as ERS, Topex/Poseidon, Jason, and Envisat. Unlike other altimetric missions, Cryosat-2 has two antennae. The SAR and SARin modes operate by transmitting bursts of pulses at a high pulse frequency (HPF), pausing to receive the returned echoes before transmitting the next pulse [29]. In SAR mode, only the antenna to the left of the flight direction is used (ibid), while for SARin, the pulse is transmitted from the left antenna but received at both. With the antenna baseline across the track, the transmitted signal will be received at different times at the two antennae if the transmission travels slightly different distances. Alternatively, this can be viewed as a phase shift between the two received signals. The phase difference between the signals for the two antennae provides information on slope-over-ice cap margins but also provides insight into the roll angle and off-pointing over oceans and inland waters, respectively, the subject of this study. The antenna design has significance within the analysis of the phase differences between the two antennae. In particular, the slightly asymmetric antenna pattern results in non-identical phases for reflections over sloping surfaces or, equivalently, with off-pointing.

This paper is structured as follows. The mathematics underpinning the beam formation of the Cryosat-2 SAR and SARin modes, and the theory is presented in Section 2, along with the power of the multi-look waveform. Expressions for the waveforms from the two antennae are used to formulate the phase difference between the waveforms. In the simplified analysis for a surface, based on a single beam so thin that it can be described by a line, the geometric considerations link the phase difference with the cross-angle and

the reflection power of the ground points. This approach provides expressions for the cross-angle of a homogeneous surface and for cases when the dominant reflection is to the left and right of the nadir point. The associated range correction for off-pointing is also considered in Section 2. The homogeneous case of Section 2 is used in Section 3 for an oceanic pass with nadir reflection to validate the approximation by recovering the satellite roll angle. For application to inland waters, the geographical locations of Cryosat-2 ground tracks across the Amazon near the river gauge at Tabatinga are presented in Section 3, along with the river mask. The main results of altimetric height correction using off-pointing are tabulated in Section 4. In that section, altimetric data over a 285 km stretch is fitted to that of the gauge at Tabatinga. In a first-order fitting procedure, the approach utilises off-pointing but also allows for the slope, reach, and river velocity of a moving wave. A further correction is subsequently used to account for inhomogeneous reflections as the radar pulse traverses the radar footprint, as well as potential error in the roll angle. Section 5 contains a discussion of the results.

2. Cryosat-2 SARin Phase: Theory

2.1. Cryosat-2 SAR and SARin Modes

In the SAR and SARin modes, the Full Bit Rate (FBR) I (in-phase carrier) and Q (quadrature-phase carrier) components of the individual echoes of the pulses for the operational antennae are telemetered to the ground. These data, along with positioning, geophysical, orbital, and other associated altimetric corrections, are provided in SAR and SARin FBR level 1A (L1A) data files. In SARin, the tracking measurement window is 240 m, compared with 60 m in SAR. Furthermore, the burst repetition interval is 46.7 ms against 11.7 ms in SAR. Thus, the burst point ground points are spaced about 80 m along-track for SAR and near 310 m in SARin. In SARin, there are 512 samples per echo, compared with 128 in SAR. Zero padding [9] is used in the SARin waveform derivation, giving 1024 samples per SARin echo. Version C SIRAL SARin Full Rate (SIR_SIN_FR) data was used in this study.

Consider an altimetric footprint with elemental scatterers, k, on the ground at location x_k and the onboard complex deramped altimetric signal [30] for burst b. Denote this as $\widetilde{\phi}_b(x_k)$. In the theoretical development, $\pm$ denote the two antennae. A SAR-only development can be inferred by taking the + antennae with the baseline distance between the antennae, $\beta = 0$. By using the along-track sampling interval and converting the additional range for each pulse in the burst to a phase shift (due to the Doppler effect from satellite motion), the complex-valued echoes can be given by

$$\phi_b^{\pm}(m) = F\left\{I_b^{\pm}(m) + iQ_b^{\pm}(m)\right\} \tag{1}$$

where F denotes the Fourier transform, $i = \sqrt{-1}$ is the imaginary number, and $m = 0, 1, \ldots, 63$ denotes the echo number in the burst centred at time t with orbital position $\underline{x}_b$. It is noted that $\underline{x}_b$ lies mid-way between the 32nd and 33rd individual start–stop locations; each start–stop location is related to an individual echo in the burst of 64 echoes [29]. The reflectors, k, on the ground are the same for each pulse due to the high repetition rate. During a burst, the carrier phase is locked to the transmission timing so that transmission within the burst is phase-coherent. After allowance for the phase shift (due to the Doppler effect from the satellite motion), the returned waveforms themselves exhibit phase coherence. Under this assumption we can represent

$$(m) = \sum_k \widetilde{\phi}_b(x_k)\, e^{\pm ik_0\beta\hat{\underline{n}}_k\cdot\frac{\hat{m}_b}{2}} e^{2i(m-\frac{63}{2})\Delta k_0\hat{\underline{n}}_k\cdot\hat{\underline{n}}_v} \; m = 0, 1, \ldots, 63 \tag{2}$$

where $\widetilde{\phi}_b(x_k)$ is the reflectance from the kth scatterer; β is the antenna baseline; $k_0 = 2\pi/\lambda$ is the carrier wave number, where λ is the wavelength of the carrier; Δ is the along-track sampling interval; $\underline{\hat{n}}_k$ is the unit vector from burst centre to the elemental scatterer; $\underline{\hat{n}}_v$ is the direction of the velocity vector; and $\underline{\hat{m}}_b$ is a unit vector in the direction of the interferometer baseline. Since the satellite moves only 310 m in SARin mode during the duration of the burst, the velocity vector is considered a straight line.

Equation (2) underpins the mathematics behind the "beam formation" stage, where we form

$$\psi_b^{\pm}(\theta_1) = \sum_{m=0}^{63} \phi_b^{\pm}(m) e^{-2ik_0\Delta\theta_1(m-\frac{63}{2})} \tag{3}$$

In Equation (3), θ_1 is called the "look-angle" of the beam, taken as

$$\theta_1 = \theta_R^b + \frac{\pi n}{64k_0\Delta} \; n = 0, 1, \ldots, 63 \tag{4}$$

where we can identify the beam inclination, $\frac{\pi}{64k_0\Delta}$.

The so-called rock-angle, θ_R^b, of Equation (4) is used to direct the beam to either the nadir-pointing direction or to pre-defined equiangular ground points [9,29]. Substituting Equation (4) into Equation (3) and rearranging gives

$$\psi_b^{\pm}(n) = \sum_{m=0}^{63} \phi_b^{\pm}(m) e^{-2ik_0\Delta\theta_R^b(m-\frac{63}{2})} e^{-\frac{2i\pi n(m-\frac{63}{2})}{64}} \tag{5}$$

The dependence of $\psi^{\pm}$ has changed from the look-angle, θ_1, of Equation (3) to the integer n, where θ_1 and n are linked by Equation (4). Using Equations (3) and (5), it can be shown that

$$\psi_b^{\pm}(n) = \sum_k \widetilde{\phi}_b(x_k) e^{\pm ik_0\beta\underline{\hat{n}}_k\cdot\frac{\underline{\hat{m}}_b}{2}} d\left(\underline{\hat{n}}_k\cdot\underline{\hat{n}}_v - \theta_R^b - \frac{\pi n}{64k_0\Delta}\right) \tag{6}$$

where

$$d(x) = \frac{sin(64\Delta k_0 x)}{sin(\Delta k_0 x)} \tag{7}$$

Equations (6) and (7) show that the echoes are a product of the echo illumination with the beam pattern [29]. This is a function of direction only. Thus, the burst beam is steered into a fan of equiangular directions for n = 0, 1, …, 63. With the satellite near 717 km in altitude and using the 3 dB antenna width, the altimetric footprint is about 13.47 km along-track and 15.04 km cross-track. We may consider beam steering to be slicing the ground footprint into 64 sections along-track, leaving the full cross-track illumination. Now, by denoting

$$\hat{\phi}_b^{\pm}(m) = \phi_b^{\pm}(m) e^{-2ik_0\Delta\theta_R^b m} \tag{8}$$

in Equation (5), we have

$$\psi_b^{\pm}(n) = e^{ik_0 63\Delta\theta_R^b} e^{\frac{i63\pi n}{64}} \sum_{m=0}^{63} \hat{\phi}_b^{\pm}(m) e^{\frac{-2i\pi nm}{64}} \; n = 0, 1, \ldots, 63 \tag{9}$$

Hence, beam formation is undertaken through multiplication (phase shift), and an FFT is used as the summation

$$\sum_{m=0}^{63} \hat{\phi}_b^{\pm}(m) e^{\frac{-2i\pi nm}{64}}$$

can be simply computed via the fast Fourier transform. The maximum angle of the beam is such that the maximum of the $(n + 1)$ beam coincides with the first zero of the nth beam; this equates to 0.0239° or, equivalently, 300 m along-track.

For each transmitted pulse, an individual look of the beam formation is steered using an appropriate rock-angle towards the 64 ground points in sight. With the orbital height of Cryosat-2, there are typically 60 SARin looks forming the stack for each ground point.

As described in [9], the looks in the stack are range- and bin-corrected, the geometric range being previously corrected for tropospheric and instrument effects. Each look is contaminated by radar speckle effects with phase incoherence between components in the stack. To overcome phase incoherence, the power, $P\psi^{\pm}_{ml}\left(\underline{x}_g\right)$, of the multi-look waveforms is derived, namely,

$$P\psi^{\pm}_{ml}\left(\underline{x}_g\right) = \frac{\sum_{i=1}^{N_{ml}} w_{b_i}\psi^{\pm}_{b_i}\left(\underline{x}_g, \Delta h_{c_{,i}}\right)\overline{\psi}^{\pm}_{b_i}\left(\underline{x}_g, \Delta h_{c_{,i}}\right)}{\sum_{i=1}^{N_{ml}} w_{b_i}} \tag{10}$$

where the summation is over the waveforms, i, for the stack at ground point $\underline{x}_g$; N_{ml} is the total number in the stack; $\Delta h_{c_{,i}}$ is the slant range correction for beam centre i; and w_{b_i} is the associated weight for the ith waveform. The bar over ψ denotes the complex conjugate. The multi-look waveforms of Equation (10) are retracked to recover the height of the water surface. As in [9], the Offset Centre of Gravity (OCOG)/Threshold Retracker [31] is used with a retracking point at 80% of the amplitude.

2.2. Cryosat-2 SARin Cross-Angle

The SARin mode is designed for recovering altimetric heights along ice cap margins where the slope of the terrain can lead to an incorrect point of closest approach (POCA). The power of the multi-look SARin waveforms of Equation (10) is recovered for both antennae separately and retracked to provide the height. Although the components of the multi-look waveforms from the two antennae are not themselves coherent, the phase difference between the components is coherent, as the phase offset between transmitted pulses is eliminated in forming the difference. For a cross-track sloping surface over ice, for example, the POCA will not be at the nadir point but at an angle to the nadir-pointing direction. For inland waters, the across-track slope of the river will be negligible, but as water is a better reflector than land, the waveform will be dominated by reflectors from the water, which can differ from the POCA. Thus, for SARin, we consider the cross-power,

$$\psi^{*}_{ml} = \frac{\sum_{i=1}^{N_{ml}} w_{b_i}\psi^{+}_{b_i}\overline{\psi}^{-}_{b_i}}{\sum_{i=1}^{N_{ml}} w_{b_i}} \tag{11}$$

the multi-look argument or phase, $A\psi_{ml}$,

$$A\psi_{ml} = Arg(\psi^{*}_{ml}) \tag{12}$$

and the multi-look coherence,

$$C\psi_{ml} = \frac{\left|\psi^{*}_{ml}\right|}{\left(P\psi^{+}_{ml}P\psi^{-}_{ml}\right)^{\frac{1}{2}}} \tag{13}$$

In a simplified analysis for a sloping surface based on a single beam so thin that it can be described by a line, and using geometric considerations, Ref. [29] developed expressions for the amplitude and phase of the cross-power over a sloping surface with zero roll angle. Of significance is the antenna pattern, as described by the gain function, G, which depends on the polar angle relative to the boresight, namely,

$$G(\theta_A, \vartheta_A) = G_0 exp\left[-\theta_A^2\left(\frac{cos^2\vartheta_A}{\gamma_1^2} + \frac{sin^2\vartheta_A}{\gamma_2^2}\right)\right] \tag{14}$$

where $\theta_A(\vartheta_A)$ is the polar(azimuthal) angle of the received signal with respect to the antenna's boresight, G_0 is the peak gain, and $\gamma_1(\gamma_2)$ is the antenna parameters with a value of 0.0133(0.0148). Under the thin-beam assumption, the expected cross-product power of the returned signal at the two antennae is

$$\left\langle \psi^{+}\overline{\psi}^{-} \right\rangle = \frac{\lambda^2 D_0 G_0^2 R}{4\pi^3 z_0^2} exp(-\frac{2\theta_1^2}{\gamma_1^2}) \int \sigma^0(\phi) exp\left(-\frac{2sin^2(\theta-\theta_r)}{\gamma_2^2 + ik_0\beta sin(\theta-\theta_r)} \right) \delta\left(t_{sl} - \frac{2}{c}\left(z_0 + \frac{\frac{2R^2}{z_0} sin^2\varnothing}{2} \right) \right) d\phi \quad (15)$$

where $D_0 = \int_{-\infty}^{\infty} d^2(u)d(u)$, λ is the radar wavelength, z_0 is the height of the satellite, θ is the cross-angle, θ_r is the roll angle, θ_1 is the along-track angle, δ is the Dirac delta function, t_{sl} is the slant range corrected time, ϕ is the geocentric angle between the satellite nadir point and the reflector, c is the speed of light, and σ_0 is the backscatter coefficient.

For inland waters (see Figure 1), the reflectors at time τ_0 may not correspond to the POCA, as the backscatter is non-uniform and dominated by water reflectors. The single-beam geometric approach is then dominated by the water side. In such cases, the multi-look waveform from a relatively narrow water body is often characterised by a quasi-specular peak over a small number of bins [9].

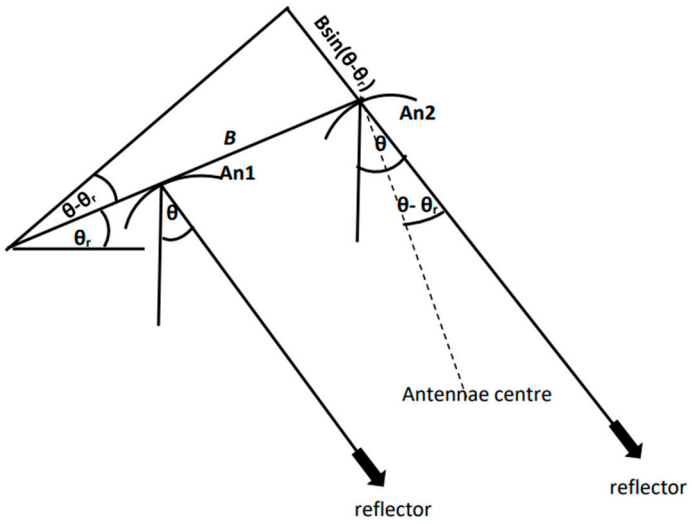

Figure 1. Schematic of reflectors in SARin waveforms: θ_r is the roll angle, θ is the incidence angle of the reflector to the nadir direction, B is the antenna baseline, $\theta - \theta_r$ is the angle between the baseline and the incident direction, and $Bsin(\theta - \theta_r)$ is the additional pathlength of the reflected signal between Antenna 2 (An2) and Antenna 1 (An1).

The reflector point for the line beam can be parameterised by the off-pointing angle, θ; the time elapsed since reflection from the nadir point, τ; or by the geocentric angle, $\varnothing$. For a level surface but a non-zero roll angle, the approach in [29] can be adapted. In particular, the argument of the Dirac delta function can be reformulated as

$$t_{sl} - \frac{2}{c}\left(z_0 + \frac{\frac{2R^2}{z_0} sin^2\varnothing}{2} \right) = \tau - \frac{4R^2\eta sin^2\phi}{cz_0} \quad (16)$$

where $\eta = 1 + \frac{z_0}{R}$ is the departure of a sphere of radius R from a plane. Thus, the point of reflection corresponds to

$$\tau \approx \frac{4R^2\eta sin^2\phi}{cz_0} \quad (17)$$

or to the first order for a spherical Earth, $sin\theta = \frac{R}{z_0} sin\phi$, giving

$$\theta \approx \pm \left(\frac{c\tau}{\eta z_0} \right)^{\frac{1}{2}} \tag{18}$$

the well-known result for the off-pointing angle being proportional to $\tau^{\frac{1}{2}}$ [32]. Let

$$\theta_+ = -\theta_- = \left(\frac{c\tau}{\eta z_0} \right)^{\frac{1}{2}} \geq 0 \tag{19}$$

denote the off-pointing angles to the left and right of the nadir, with $\sigma_\pm = \sigma_0(\theta_\pm)$ as the corresponding backscatter coefficients at the ground reflectors; then,

$$\begin{aligned} \left\langle \psi^+ \overline{\psi}^- \right\rangle = \frac{\lambda^2 D_0 G_0^2 R}{4\pi^3 z_0^2} exp(-\frac{2\theta_1^2}{\gamma_1^2}) exp(-\frac{2(\theta_+^2+\theta_r^2)}{\gamma_2^2}) * \sigma_+ e^{-\hat{c}} cos(k_0\beta(\theta_+ - \theta_r)) + \\ e^{-\hat{c}} cos(k_0\beta(\theta_+ + \theta_r)) + i\{\sigma_+ e^{\hat{c}} sin(k_0\beta(\theta_+ - \theta_r)) - \sigma_- e^{-\hat{c}} sin(k_0\beta(\theta_+ + \theta_r))\} \end{aligned} \tag{20}$$

where

$$\hat{c} = \frac{4\theta_+\theta_r}{\gamma_2^2} \tag{21}$$

Using small-angle approximations in Equation (20),

$$tanarg\left\langle \psi^+ \overline{\psi}^- \right\rangle \approx \left[\left(\sigma_+ e^{\hat{c}} - \sigma_- e^{-\hat{c}} \right) k_0\beta\theta_+ - \left(\sigma_+ e^{\hat{c}} + \sigma_- e^{-\hat{c}} \right) k_0\beta\theta_r \right] / \left(\sigma_+ e^{\hat{c}} + \sigma_- e^{-\hat{c}} \right) \tag{22}$$

which simplifies to

$$\frac{tanarg\left\langle \psi^+ \overline{\psi}^- \right\rangle}{k_0\beta} + \theta_r \approx \theta_+ \left(1 - \frac{2\sigma_- e^{-\hat{c}}}{\sigma_+ e^{\hat{c}} + \sigma_- e^{-\hat{c}}} \right). \tag{23}$$

Equation (23) can be further simplified in three cases:

(i) The reflective surface is symmetrically homogeneous, $\sigma_+ = \sigma_-$;
(ii) The reflection is dominant on the + side, $\sigma_+ \gg \sigma_-$;
(iii) The reflection is dominant on the − side, $\sigma_- \gg \sigma_+$.

Case (i) reduces to

$$tanarg\left\langle \psi^+ \overline{\psi}^- \right\rangle \approx -k_0\beta\theta_r + k_0\beta\theta_+ tanh(\hat{c}). \tag{24}$$

For a nadir reflection, as with over oceans, $\hat{c} = 0$, and Equation (24) provides a means for determining the roll angle (next section). For a small $\hat{c}$, that is, non-zero cross- and roll angles, Equation (24) is analogous to [29] on using Equations (18) and (21), namely,

$$tanarg\left\langle \psi^+ \overline{\psi}^- \right\rangle \approx -k_0\beta\theta_r + k_0\beta \frac{4c\tau\theta_r}{\eta z_0 \gamma_2^2} \tag{25}$$

Thus, for a homogeneous surface, the argument is linear in time, with the temporal rate of change positive if the roll angle is positive due to the antenna gain giving greater weight to the antenna closest to the antenna boresight. The linear variation is due to small differences in phase between the pair of points resulting from the differential effect of the gain pattern of the antennae. Although applicable to oceans and ice surfaces over inland waters, cases (ii) and (iii) are more relevant. In case (ii), to first order in $\frac{\sigma_-}{\sigma_+}$,

$$\frac{tanarg\left\langle \psi^+ \overline{\psi}^- \right\rangle}{k_0\beta} + \theta_r = \theta_+ \left(1 - 2\frac{\sigma_-}{\sigma_+} e^{-2\hat{c}} \right) \tag{26}$$

Analogously, in case (iii), to first order in $\frac{\sigma_+}{\sigma_-}$,

$$\frac{tanarg\left\langle \psi^+\overline{\psi}^- \right\rangle}{k_0\beta}+\theta_r = \theta_-\left(1-2\frac{\sigma_+}{\sigma_-}e^{2\hat{c}}\right) \tag{27}$$

on using $\theta_- = -\theta_+$.

Equations (21), (26) and (27) can be combined as

$$\frac{tanarg\left\langle \psi^+\overline{\psi}^- \right\rangle}{k_0\beta}+\theta_r = \theta\left(1-2\hat{\sigma}e^{\frac{-8\theta\theta_r}{\gamma_2^2}}\right) \tag{28}$$

where θ is the cross-angle, and $\hat{\sigma}$ is the ratio of the sigma noughts with the weaker reflection, determined by the sign of θ as the numerator. In both cases (ii) and (iii), the effect of the weaker reflection is to increase the magnitude of the offset angle. Conversely, neglecting the weaker reflection leads to a small underestimation of the magnitude of the offset angle.

2.3. Altimetric Corrections for Non-Zero Cross-Angle

A non-zero cross-angle, θ, indicative of off-pointing to non-nadir inland water reflectors, has consequences for the water height and the water location. Without considering the cross-angle, the altimetric range, l, from the satellite to the water body is assumed to be in the nadir direction. If the true nadir distance is N, then the required water height correction is $\Delta = l - N$, where (Appendix A)

$$\Delta \approx 2lsin^2\frac{\theta}{2}+\frac{l^2}{2R}sin^2\theta. \tag{29}$$

Δ can be subtracted from the slant range to recover the range to the water surface or, alternatively, added to the retracked inland water height measurement to yield the required height of the water body. As seen later, this correction can be as large as 60 m.

Similarly, the water body will be incorrectly geolocated and possibly misclassified as being over land if a water body mask is employed. Let ζ be the geocentric angle given by

$$sin(\zeta) = lsin(\theta)/R \tag{30}$$

Then, the latitude and longitude of the water reflectors can be found rigorously using spherical trigonometry (Appendix B) or approximately in near equatorial regions for Cryosat-2 by using a polar orbit approximation. In the latter case, the latitude is that of the sub-satellite point, while the longitude changes by $\pm\zeta$, where the + sign is taken for descending arcs and the minus sign for ascending arcs, given the convention that the phase difference is that of left minus right antennae.

3. SARin Phase Analyses

3.1. SARin Cross-Angle over Ocean

Equations (11)–(13) are essentially those in [29] except that cosine weighting within the multi-look waveforms is included in Equation (11) rather than unit weighting. The denominator in Equation (13) utilises the power of both antennae so that $C\psi_{ml} = 1$ if $\psi^+_{b_i} = \psi^-_{b_i}$ for all waveforms, i, in the stack. Ref. [29] proposed determining the phase difference from Equation (12) by minimising the functional,

$$\frac{C\psi^3_{ml}(\tau)}{1-C\psi_{ml}(\tau)}(A\psi_{ml}(\tau)-g(\tau,\chi))^2 \tag{31}$$

with respect to parameters $\chi = \{\chi_1, \chi_2\}$, where (c.f. Equation (24))

$$g(\tau, \chi) = \begin{cases} \chi_1 \ \tau < \tau_0 \\ \chi_1 + \chi_2(\tau - \tau_0) \ \tau > \tau_0 \end{cases} \tag{32}$$

In Equation (32), τ_0 is the time determined from the range retracker. After determining χ_1, the computed roll angle is recovered from

$$\theta_r = -\left(\frac{\chi_1}{k_0 \beta}\right) \tag{33}$$

Validation of the cross-product approach to determine the roll angle is provided by a single pass of oceanic L1A SARin FBR data on 28 April 2011, offshore of the Amazon estuary (Figure 2). Cryosat-2 passed N-S, starting over the ocean, approaching land south of the Amazon estuary. For this pass, the roll angle of the altimetric data is $\approx -0.175^\circ$. We processed data from each antenna using the OCOG/Threshold Retracker. Figure 3 shows two waveforms, their coherence, and phase differences from locations along the ocean segment of over 1000 points. The points were chosen arbitrarily, but other points gave similar plots. The top subplots show the waveforms from the right and left antennae. There are differences over the trailing edges, but the leading edges are almost identical. The middle plots show the coherence (Equation (13)). At the POCA (near bin 512), the coherence is ≈0.84 for both locations. Again, this is replicated in all other oceanic locations along this pass. The lower plot shows the phase difference between the complex values in the respective bins of the two antennae's waveforms. The phase difference oscillates wildly in the signal noise of the first 490 bins. From bin 490 onwards, the phase change is coherent. At bin 800, the phase jumps from -180° to $+180^\circ$. χ in Equation (32) is derived from bins ≈490–530 upon taking 20 bins on either side of the tracked point. The near constancy before the tracked point and monotonic decrease afterwards is evident in the phase plots. As the oceanic surface is level, χ_1 is positive, and hence, χ_2 is negative (Equation (24)). All oceanic points show the same negative slope after about bin 512, as seen in Figure 3. Figure 4 shows the difference between the Geophysical Data Record (GDR) roll angle and that from the cross-product for all points along the ocean pass; the dashed line is the GDR roll angle. South of latitude 0.4°N, the difference deviates rapidly from zero when the satellite is over land. The procedure has corrected for the non-zero roll, giving a POCA at the satellite nadir point. Over latitude 0.4–3.0°, the mean roll angle offset from the GDR value is $-0.0003^\circ \pm 0.0002^\circ$ at 95% confidence. As the formulism of Equation (32) is inapplicable for small inland waters where the waveform footprint involves water and land reflectors, an alternative approach is adopted, namely, taking χ_1 as the average of $A\psi_{ml}(\tau)$ of Equation (12) across three bins centred on τ_0. Coherence is not used directly but as a quality control on the viability of the input phases. Using the 3-bin average centred on the retracked point, the mean roll angle difference over latitude 0.4–3.0° is $-0.0034^\circ \pm 0.0003^\circ$ at 95% confidence.

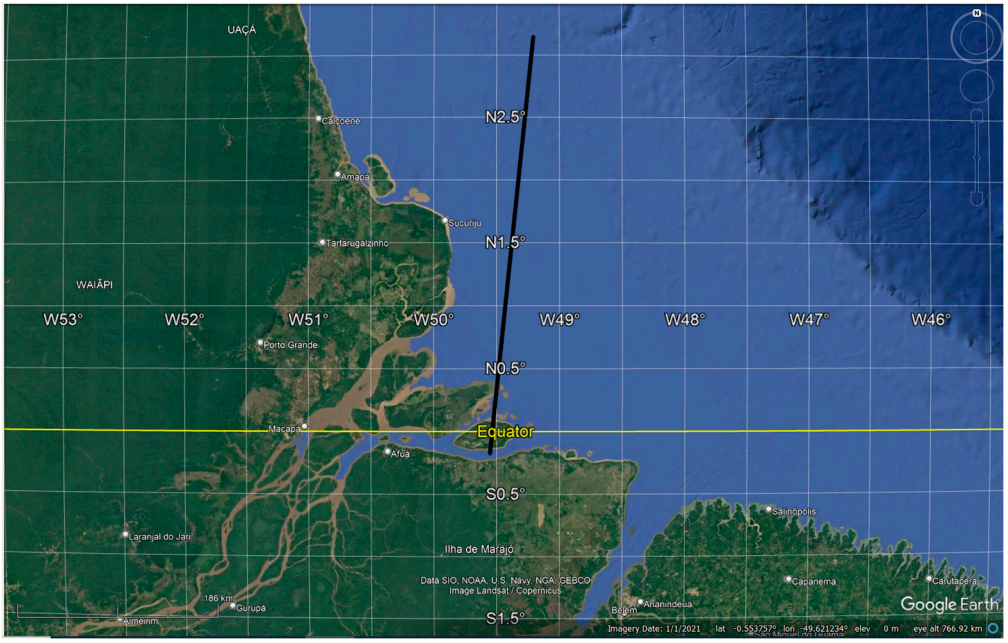

Figure 2. Google Earth image of Cryosat-2 descending pass on 28 April 2011 off the Amazon estuary. Cryosat-2 pass: 3.1481°N, 49.2059°W to 0.1728°S, 49.5516°W.

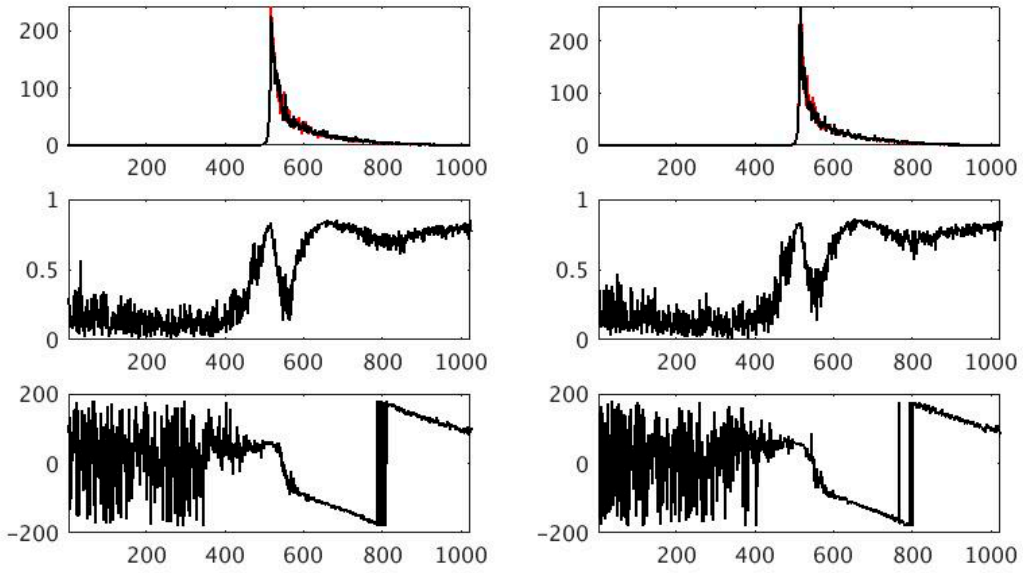

Figure 3. Top plot: Power of multi-look waveforms from the two Cryosat-2 antennae (red and black curves). Middle plot: Coherence. Lower plot: Phase differences between antennae over the bins (deg). Left plots for oceanic location 1.7907°N, 49.3472°W; right plots for oceanic location 1.2465°N, 49.3038°W.

3.2. SARin Cross-Angle over Amazon near Tabatinga

Cryosat-2 operates in SARin mode in a region across the Solimões–Amazon from approximately −75° to −63°E, −6° to +3°N. The region from 70.37° to 69.30°W and 4.45° to 3.75°S is centred near the gauge at Tabatinga, 69.933°W, 4.25°S (Figure 5). Around Tabalinga, the river width is 1–1.5 km [33]. A river mask for this 285 km stretch of the Amazon was derived by merging relevant tiles of the SRTM Water Body Dataset before manually removing water bodies, such as small lakes and tributaries, that are not part of the main river channel. SRTM data was collected from 11 to 22 February 2000. JRC (https://global-surface-water.appspot.com, accessed on 19 March 2020) has published [34]

global water occurrence maps using Landsat images. The metadata provides the occurrence of water as a percentage. Figure 6 shows that the SRTM (red curve) is a close match at locations that are classified as water in ~50% of the JRC images, although some points are missed in the SRTM masks. Use of any mask is imperfect, as the data is a temporal snapshot of the river dynamics compared to a static or probabilistic river mask. Based on the SRTM river mask, indices mask_nadir and mask_offset were allocated a value of unity for the Amazon River at the nadir and at the derived cross-angle ground point, respectively; otherwise, the value is zero.

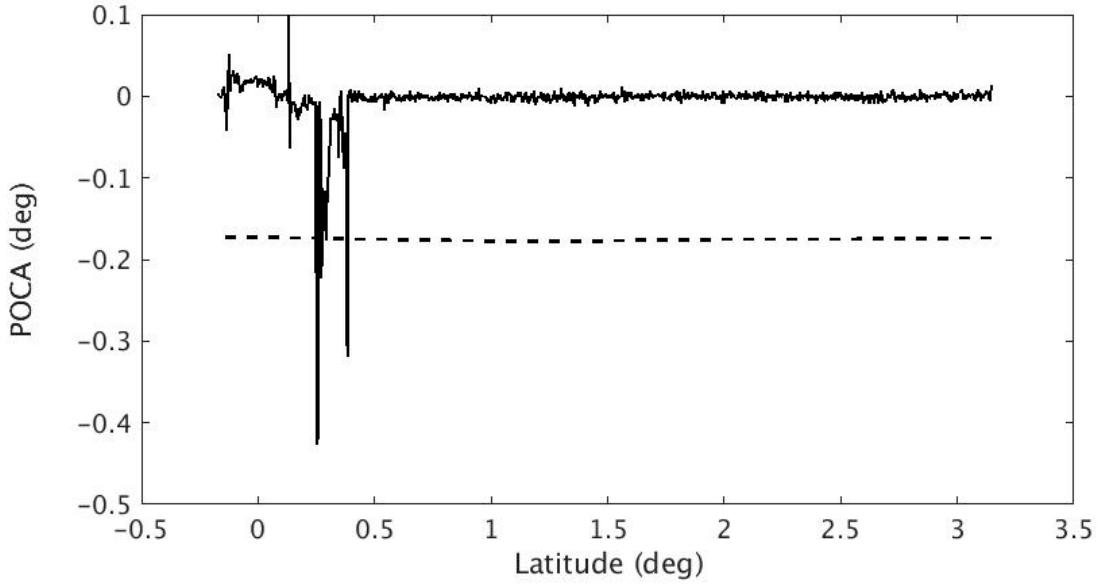

Figure 4. Difference (solid curve) between roll angle derived from the cross-product and the GDR roll angle (dashed curve) for ocean pass (north to south) of 28 April 2011. Sub-satellite points over land below latitude 0.4°N.

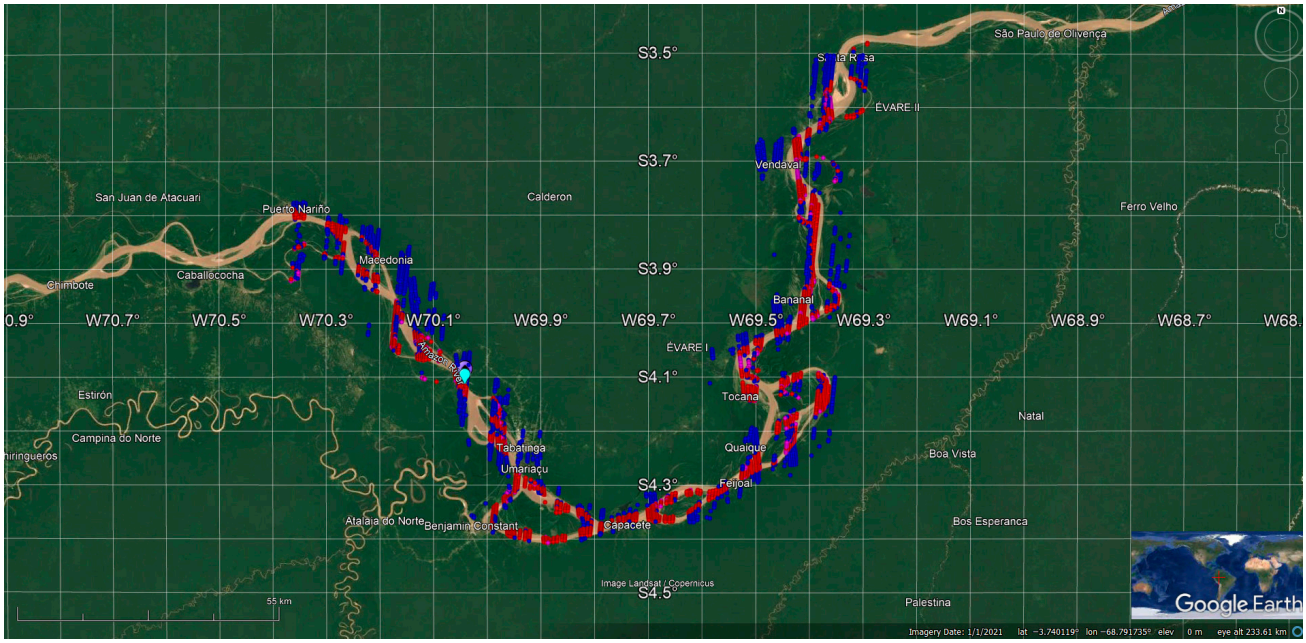

Figure 5. Cryosat-2 crossings of the Amazon in the vicinity of the gauge at Tabatiga (cyan pin), with points at the nadir red (mask_nadir = 1; mask_offset = 1) and purple (mask_nadir = 1; mask_offset = 0), and off-pointing reflectors blue (mask_nadir = 0; mask_offset = 1).

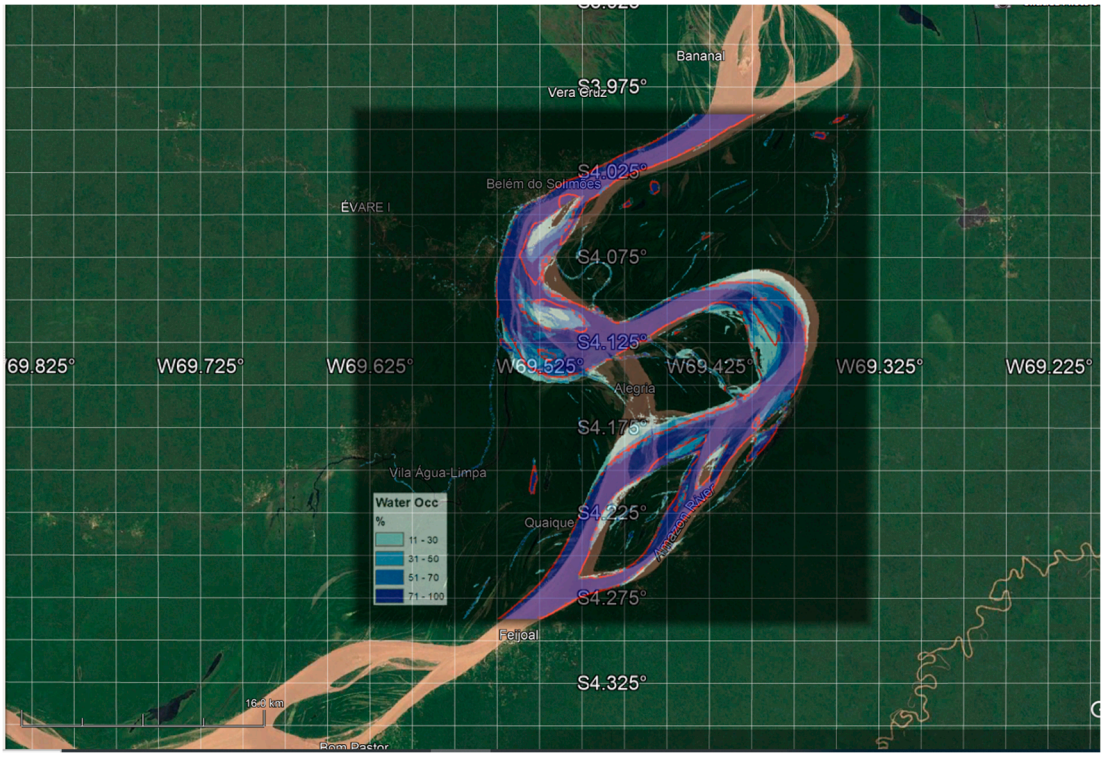

Figure 6. Comparison of SRTM river mask (red curve) and probabilistic water occurrence [34] of the Amazon overlaid on a Google Earth image.

Figure 5 shows a total of 253 passes across the Amazon, some of which cross at several locations. In total, 3416 points had an inland water location at the nadir, with a further 2399 non-nadir locations identified as being from the Amazon. The cross-angle was inferred from Equation (26) or Equation (28) from the multi-look waveform of Equation (12). Given the uncertainty in the sigma noughts, the cross-angle was estimated by neglecting the effect of the secondary reflection, hence assuming that the reflection is totally that of the water. As a detailed illustration, consider the descending pass on 5 October 2012 (Figure 7) spanning 120 km. There are 109 river points at the nadir, with a further 61 using cross-angle off-pointing. Figure 8 plots the power, coherence, and cross-angle against the bin number for typical off-nadir and nadir water reflections. For the nadir water reflectors, the retracking point is near bin 514, with bins 513–515 averaged for the off-pointing angle. Coherence is consistent across the bins, with the cross-angles close to zero. In contrast, for the river off-nadir, the power shows low power reflectance at the nadir near bin 485, with the retracked river signature centred near bin 530. Coherence is above 0.8 at the two reflections. The bin cross-angle is zero at the nadir but 0.13° at bin 530.

Figure 7. Google Earth plot of north-to-south (descending) Cryosat-2 ground-track of 5 October 2012. Locations with river at the nadir are red (mask_nadir = 1; mask_offset = 1) and purple (mask_nadir = 1; mask_offset = 0), and off-pointing reflectors are shown blue (mask_nadir = 0; mask_offset = 1).

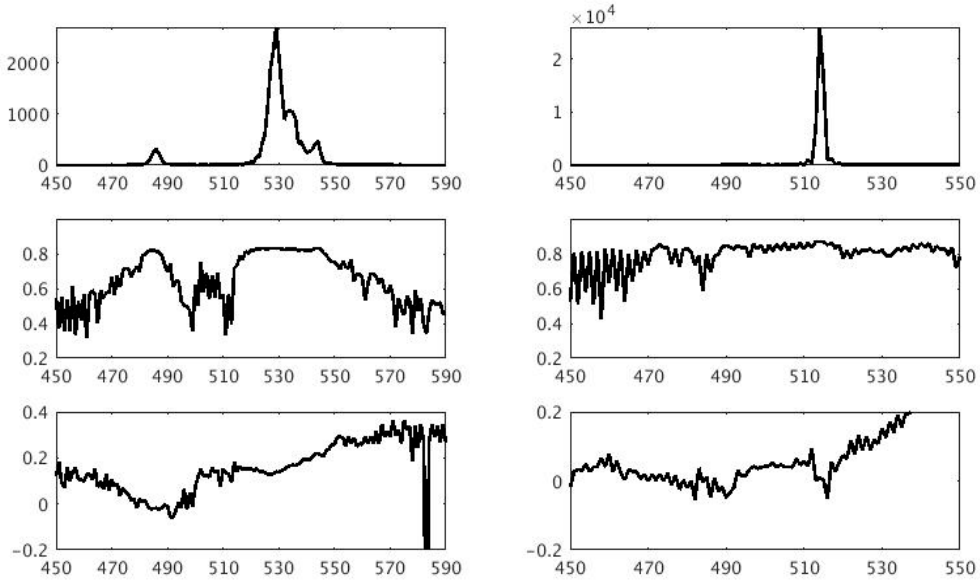

Figure 8. Top plot: Power of multi-look waveform from the Cryosat-2 left antenna. Middle plot: Coherence. Lower plot: Cross-angle (deg) derived from phase differences. Left/right plots for first off-pointing/nadir locations in Figure 7.

4. Results

4.1. River Height

SAR altimetry is pulse-limited across-track with reflectors closer to the nadir, providing, in general, greater power than reflectors displaced across-track. Furthermore, with Cryosat-2 having a negative roll angle in Equation (17) (range $-0.16°$ to $-0.17°$), the phase difference needs to be equal but of opposite sign to the roll for nadir reflectance. Thus, along with the phase difference limited to $\pm 1.2°$ by the wavelength of the altimeter (to avoid ambiguity due to phase wrapping), but reduced by the antenna gain [29], the cross-angle is expected to be predominantly negative, assuming a random distribution of water targets across-track. In consequence, off-nadir ranging is more likely to be to the right of the nadir point as viewed along the flight path. For example, of the passes considered near Tabatinga, there are 566(308) points on descending(ascending) tracks with a cross-angle less than $-0.2°$, but only 96(2) on descending(ascending) passes with a cross-angle exceeding $0.2°$. The larger number of descending values, as shown in the pass of Figure 7, is due to the river flowing approximately NNE, closely mirrored by the Cryosat-2 descending pass ground track. The roll angle for 5 October 2012 was $-0.1682°$.

In terms of validation of altimetric river heights, the drifting orbit of Cryosat-2 complicates comparison against the Tabatinga gauge both spatially and temporally. The time of each water height was associated with a corresponding time at the gauge by using the reach between the altimetric point and gauge with the river velocity estimated within a least squares procedure, alongside a constant slope for changing river topography. The observation equation for each altimetric height at time t_i can be written as

$$h^{alt}(t_i) + \Delta = h_o + h^{gauge}\left(t_i - \frac{r_i^g}{V}\right) - sr_i^g - l\left(\delta\theta_r + 2\theta\hat{\sigma}e^{8\theta\theta_r/\gamma_2^2}\right)\left(sin\theta + \frac{lsin2\theta}{2R_e}\right) \quad (34)$$

where $h^{alt}(t)$ is the retracked altimetric river height at time t, h_0 is the datum offset between the gauge and the geoid, $h^{gauge}(t)$ is the gauge measurement, r_i^g is the reach between the altimetric point and the gauge, V is the mean river velocity, s is the mean slope, $\hat{\sigma}$ is the ratio of σ_0 in either Equation (26) or Equation (27), and $\delta\theta_r$ is the roll angle correction. Δ is the correction of Equation (18), which modifies h^{alt} to compensate for the cross-angle. With the reach spanning 56.3 km upstream to 229.1 km downstream of the gauge and assuming a velocity of 6.48 km/h (1.8 m/s), any wave moving downstream is observable for 44 h.

Table 1 summarises results from the least-squares analysis, as estimated from all 253 passes. The notation for the solutions denotes the run index, followed by the number 3, 4, or 5 after the underscore, denoting the number of parameters in the least squares solutions. A three-parameter run solves for $h_o, V,$ and s, with the solution for $\delta\theta_r$ added for a four-parameter solution and $\delta\theta_r$ and $\hat{\sigma}$ in the five-parameter solution. Also given are results from 26 passes crossing the Amazon between $-69.53°$ and $-69.29°$W and $-4.32°$ and $-3.49°$N, including the pass of Figure 8. These comprise 19 descending passes and 7 ascending passes, covering a 120 km stretch. In Table 1, the first index of the binary mask pair refers to the nadir direction, with 1 denoting that the mask detects water present at nadir, 0 otherwise. The symbol # indicates either 0 or 1. Analogously for the second index, unity denotes that the mask identifies a water reflection at the offset angle and 0 otherwise, with # indicating either 0 or 1.

Table 1. Results for 8 solutions based on SRTM river mask. Errors are 1σ.

Run	Mask	Min/Max Gauge (km)	N_{max}	N_{used}	Offset Δ (m)	Slope (m/km)	Velocity V (m/s)	$\delta\theta_r$ (deg)	$\sigma^{\pm}$	RMSE (m)
No corr	1#	−50.2/229.1	3415	3153	57.435 ± 0.008	0.03513 ± 0.00010	1.7909 ± 0.0007			0.423
i_3	1#	−50.2/229.1	3415	3215	57.498 ± 0.007	0.03504 ± 0.00009	1.7920 ± 0.0006			0.408
i_4	1#	−50.2/229.1	3415	3208	57.507 ± 0.007	0.03508 ± 0.00009	1.7962 ± 0.0006	−0.0036 ± 0.0078		0.404
ii_3	#1	−56.3/229.1	5529	5232	57.555 ± 0.007	0.03502 ± 0.00009	1.8242 ± 0.0013			0.524
ii_4	#1	−56.3/229.1	5529	5258	57.586 ± 0.008	0.03504 ± 0.00009	1.8132 ± 0.0013	−0.0033 ± 0.0018		0.527
ii_5	#1	−56.3/229.1	5529	5256	57.589 ± 0.008	0.03507 ± 0.00009	1.8209 ± 0.0007	−0.0030 ± 0.0024	0.0004 ± 0.0001	0.525
iii_3	11	−50.2/229.1	3122	2981	57.497 ± 0.008	0.03504 ± 0.00010	1.7932 ± 0.0006			0.408
iii_4	11	−50.2/229.1	3122	2976	57.505 ± 0.008	0.03508 ± 0.00010	1.7965 ± 0.0006	−0.0031 ± 0.0089		0.404
iv_3	01	−56.3/225.7	2397	2286	57.613 ± 0.014	0.03485 ± 0.00016	1.9028 ± 0.0030			0.683
iv_4	01	−56.3/225.7	2397	2301	57.703 ± 0.015	0.03483 ± 0.00016	1.8862 ± 0.0018	−0.0040 ± 0.0018		0.664
iv_5	01	−56.3/225.7	2397	2304	57.735 ± 0.016	0.03484 ± 0.00016	1.8898 ± 0.0018	−0.0029 ± 0.0030	0.0013 ± 0.0002	0.664
No corr	1#	84.2/204.9	1598	1465	57.383 ± 0.011	0.03446 ± 0.00031	1.7756 ± 0.0007			0.415
v_3	1#	84.2/204.9	1598	1483	57.471 ± 0.010	0.03461 ± 0.00027	1.7780 ± 0.0006			0.371
v_4	1#	84.2/204.9	1598	1483	57.480 ± 0.010	0.03462 ± 0.00027	1.7821 ± 0.0006	−0.0028 ± 0.0091		0.370
vi_3	#1	84.7/204.5	2410	2293	57.240 ± 0.010‘	0.03250 ± 0.00027	1.7556 ± 0.0008			0.476
vi_4	#1	84.7/204.5	2410	2285	57.246 ± 0.010	0.03258 ± 0.00028	1.7608 ± 0.0007	0.0009 ± 0.0003		0.46.9

A rejection criterion at 3σ was employed throughout to remove gross outliers. The first row summarises a run without any cross-track correction applied. This run is the standard altimetric approach, assuming all observations are from the nadir. In Run (i), the cross-track correction has now been applied. It can be seen that allowing for the point of reflection to be off-nadir, even though there is water at the nadir, improves the RMSE of fit from 0.423 m to 0.408 m, with an additional 38 measurements accepted. Run (ii) includes all points with offset water reflection. Utilising the cross-angle and river mask to identify a water reflection, as in Run (ii), yielded nearly 66% more accepted measurements (cf. Run (ii_4) and run with no correction) at the expense of a reduced accuracy of RMSE 0.527 m due to deficiencies in the correction procedure.

Neglecting the small number of (1,0) data points, as in Run(iii), implies water reflections at both the nadir and in the cross-angle direction, i.e., (1,1) pairing. Of the 349 (1,0) points, just fewer than 100 are accepted in Run (i) and have a negligible impact on the RMSE, as seen in the identical RMSE values of Run(i) and Run (iii). Run (iv) utilised observations with pairing (0,1), that is, where the SRTM mask failed to identify water at nadir, but the waveforms still provided a measurement cross-track. It is these data points that require slant range corrections at the metre to decametre level. It was hardly surprising that the four-parameter solution yielded a relatively large RMSE of 0.664 m. Data not included in the least-squares procedure was included with zero weights to recover the residuals.

Runs (v) and (vi) are for the reduced stretch of the river in Figure 8. The cross-angle and residuals after the fit of all the data points are shown in Figure 9 for the 5 October 2012 pass of Figure 8. The figure shows that the residuals of Run (vii) are now small, even for large crossover angles, while the off-pointing corrections have benefited all data, including the ground points with the river at the nadir.

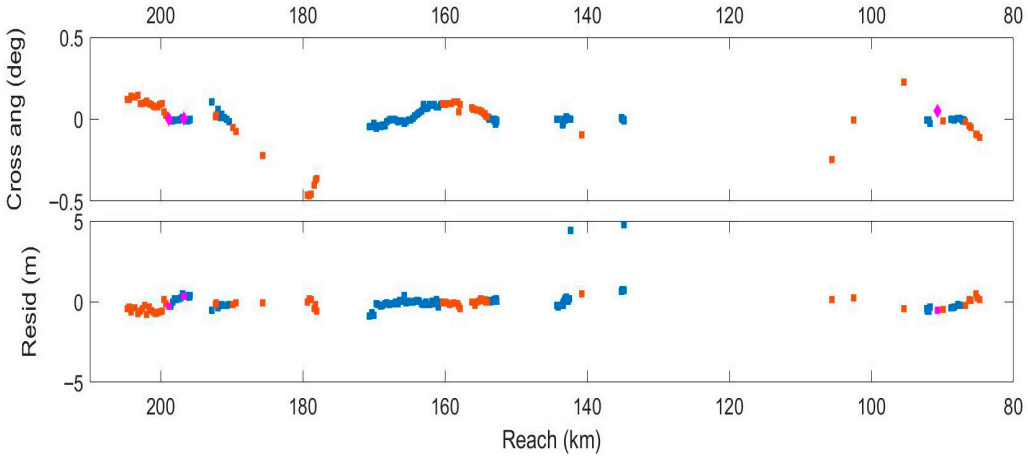

Figure 9. Upper plot: Cross-angles (deg). Lower plot: Residuals for Amazon heights for descending pass on 5 October 2012. Blue points, river at nadir (mask_nadir = 1; mask_offset = 1) and magenta (mask_nadir = 1; mask_offset = 0) red points, river off-nadir (mask_nadir = 0; mask_offset = 1). River at nadir but non-zero cross-angle indicates reflection off-nadir.

Figure 10 shows the residual from Run (ii_3) after the fit relative to Equation (34). The black dots denote water at the nadir and off-nadir (i.e., mask pair 1,1), with off-nadir river points in red (i.e., mask pair 0,1). Also shown in magenta are the unused points with mask pair (1,0). These are points in the mask identifying water at the nadir, but off-pointing identifies the reflection from a non-water surface. Such points are excluded from Runs (ii–iv). Note that the (1,0) and (1,1) pairs are clustered around zero.

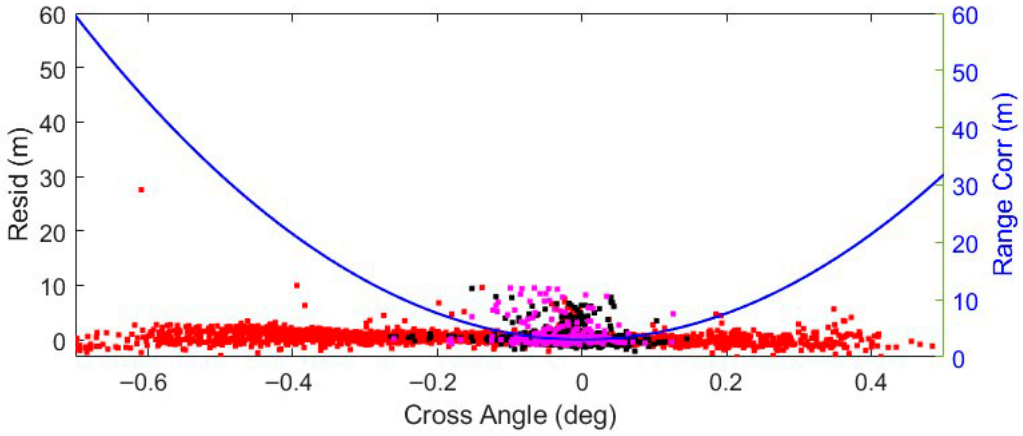

Figure 10. Residuals from Run (ii_3) plotted against the cross-angle. The black dots denote water at the nadir and off-nadir (i.e., index pair (1,1)), with off-nadir river points for index pair (0,1) in red. The latter occurs at high cross-angles. The index pair (1,0), that is the mask indicates river at nadir but the reflection at the off-nadir point is non-river, are shown as magenta dots. The range correction (shown as blue) curve is for a mean height of 717 km. This correction can exceed 60 m when the cross-angle is large and negative, with a 20 m correction for a cross-angle of $\pm 0.4°$.

The cross-angles for points with water at the off-nadir in Figure 10 cover $-0.712°$ to $0.484°$. Clearly evident is the bias towards negative values, as the roll angle is negative. The range corrections to a nadir (Equation (29)) of up to 60 m for large negative cross-angles reduce the residuals to close to that achieved for the nadir points, but, as shown in Figure 11, the residuals for the larger positive and negative cross-angles show a greater scatter in general, as expected due to off-pointing corrections of over 20 m. Both figures show a cluster of poorly determined nadir points with a scatter not observed at other angles. The reason for this becomes apparent in Figure 12, where the Run (ii_3) residuals are plotted against the month in the year. High residuals are predominantly in July–November, the dry season, during which the width of the Amazon reduces.

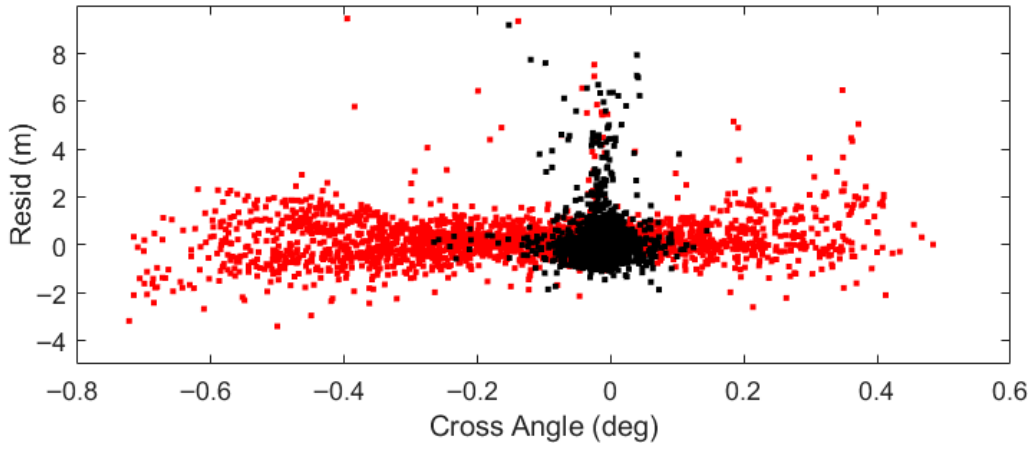

Figure 11. Residuals from Run (ii_3) plotted against cross-angle. The black dots denote water at nadir and off-nadir (i.e., index pair (1,1)), with off-nadir river points for index pair (0,1) in red.

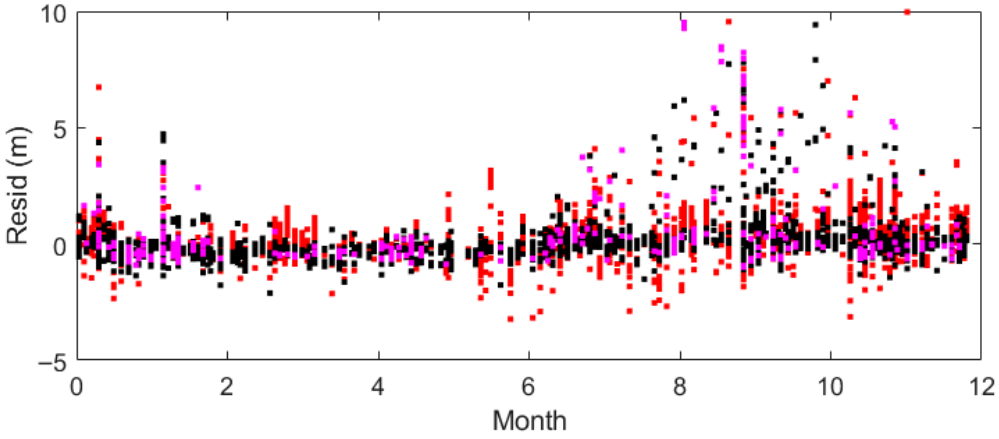

Figure 12. Residuals from Run (ii_3) plotted as a function of months of the year as measured over the range 0–12. The preponderance of high positive residuals occurs during the dry season; (1,1) nadir river points, black; (0,1) off-nadir river, red; and (1,0) nadir river but off-nadir non-river, magenta.

Analysis of the observations with absolute residuals exceeding 2 m identifies 145 in July–November, inclusive, compared with 48 for the other seven months. Restricting data in Run ii_3 to two batches, July–November and January–June and December, inclusive, gave RMSEs (m) (accepted observations) of 0.536(2630) and 0.461(2617). The number of rejected measurements was 173 for July–November and 91 for the other seven months, showing that the low-flow months are more problematic than medium to high flow.

4.2. River Slope and Velocity

The least-squares solution included a constant longitudinal river slope andvelocity over the 285 km stretch for multi-year seasonal data. Given the bias towards points downstream of the gauge, the slopes for Runs (i)–(iv) are relative to a point 70 km downstream of the gauge, with Runs (v) and (vi) to a point 144 km downstream of the Tabatinga gauge. The upper plot of Figure 13 from Run (ii_3) shows the cross-angles as a function of reach. There is no discernible pattern to the (0,1) points. The lower plot of Figure 13 confirms the near uniformity of the slope, with no discernible difference between locations over 170 km downstream or in the stretch 56 km upstream of the gauge. The assumption of constant slope is necessary over a short stretch. All slope solutions in Table 1 for the 285 km stretch are consistent within the error bars, with a typical value of 0.03506 ± 0.00004 m/km giving an overall drop in height of 10 m over the stretch. Use of data in runs (vi) and (vii) for a 120 km reach provided a smaller slope of 0.03250 ± 0.00027 m/km (Run iv_3), with the increased error bar a reflection of both the reduced data and reduced height variation of less than 4 m along the reach. The mean observed water velocity near Tabatinga was estimated to be 1.803 ± 0.014 m/s. As a single stream velocity was employed in the altimetric analysis, the derived result will be averaged across multiple years and seasons.

4.3. Roll Angle and Sigma Nought

Table 1 provides values of $\delta\theta_r$ and $\hat{\sigma}$ for the five-parameter solutions for two runs, (#,1) and (0,1), that is with the full off-pointing range included. The results show that the estimation of the roll angle correction has minimal effect on the overall solution accuracy or the number of observations included. Table 1 reveals a correction of just $-0.0030^\circ \pm 0.0024^\circ$ for the roll angle.

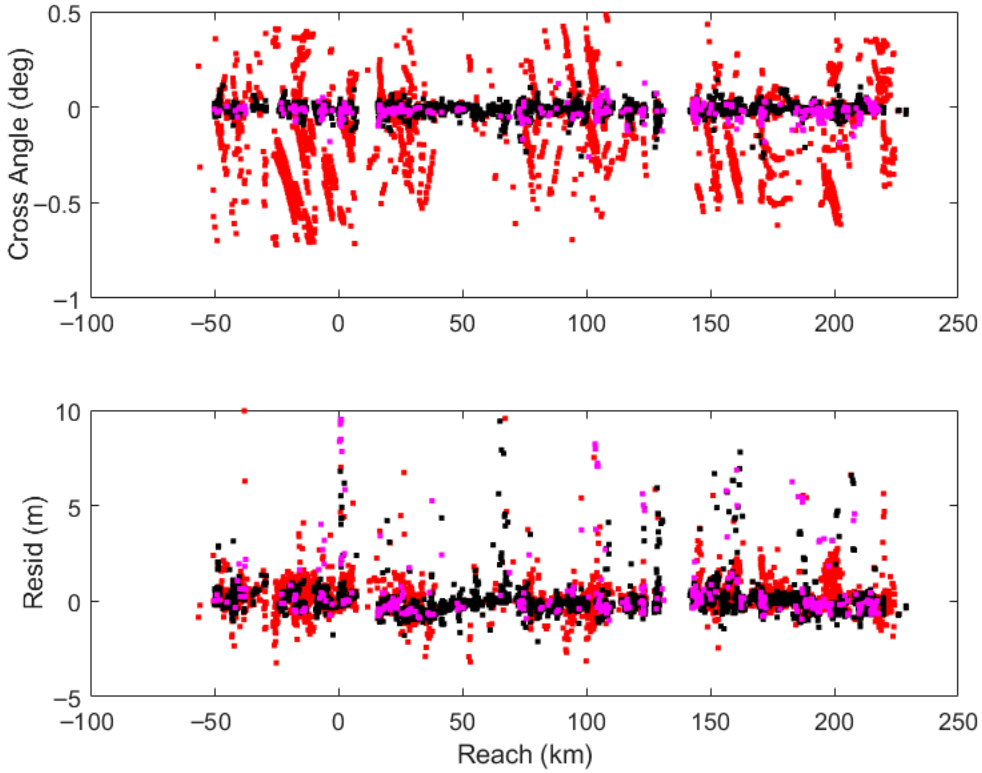

Figure 13. Cross-angles (upper plot) and residuals (lower plot) for altimetric Amazon heights as a function of the 285 km reach relative to the gauge at Tabatinga. (1,1) nadir river points, black; (0,1) off-nadir river, red; and (1,0) nadir river but off-nadir non-river, magenta.

For a physically meaningful value, $\hat{\sigma}$ is positive. Negative or insignificant values were recovered from the solutions with data only at the nadir, that is, (1,#), but they were positive whenever the reflection point was off-nadir: the (#,1) and (0,1) pairs. These are the points with the largest off-pointing angles (Figure 10), as required in Equation (28), where large negative values provide a very small but just about discernible signature. With the sub-satellite nadir point not over the Amazon, as in the (0,1) pair, the data is the most likely to provide reflectors either side of the nadir, with one water and the other non-water, as required for a small $\hat{\sigma}$. Points with a small cross-angle, typified by the (1,0) and (1,1) pairs, contribute little.

5. Discussion

Cryosat-2 interferometric SAR altimetry enables estimation of the cross-track off-pointing angle from the nadir. Corrections for off-pointing are twofold, namely, the altimetric range and the water reflector location. The theoretical approach here for the cross-angle estimation has been formulated for heterogeneous sigma noughts, on either side of the nadir, and for the two cases to the left and right of the nadir when the water sigma nought is far greater than that at the reflection point on the other side. The theoretical approach was demonstrated by recovering the roll angle over an ocean pass in Section 3.1. For an oceanic pass, the reflection is at the nadir, and hence, the cross angle is essentially the roll angle. After recovery, the mean roll angle difference over latitude 0.4–3.0° is $-0.0003° \pm 0.0002°$ at 95% confidence. The negative mean is a consequence of the near-identical phase plots and the slope often commencing just before the retracked point. The formulism of Equation (32) is, however, inapplicable for small inland waters, where the waveform footprint involves water and land reflectors. Thus, for inland waters, an alternative approach was adopted, namely by taking χ_1 as the average of $A\psi_{ml}(\tau)$ in Equation (12) across three bins centred

on τ_0. The coherence of Equation (13) is not used directly but as a quality control on the viability of the input phases. If the 3-bin average centred on the retracked point is utilised for the ocean pass, the mean roll angle difference over latitude 0.4–3.0° will be $-0.0034° \pm 0.0003°$ at 95% confidence.

Over inland waters, the range of cross-angles within the recovery procedure is affected by the roll angle, with a predominance of data points, with a negative cross-angle corresponding to a negative roll angle. Range corrections to the water reflection can exceed 60 m with a 20 m correction for a cross-angle of $\pm 0.4°$. Such large corrections can introduce an additional error source into the altimetric height.

The procedure was applied to a 285 km stretch of the Solimões–Amazon, from 56 km upstream to 229 km downstream of the gauge at Tabatinga. With Cryosat-2 in essentially a non-repeat period, and given the extent of the stretch, the altimetric height model needed to include the cross-angle correction, river slope, velocity, and datum offset. In addition, a correction for the roll angle and the ratio of sigma noughts could be included in the solution. Interestingly, by allowing for a non-zero cross-angle, the overall degree of fit showed an improved RMSE difference between gauge and altimetry, from 0.423 m for the standard altimetric approach to 0.404 m when off-pointing is taken into account for nadir water reflections. Even for supposed nadir inland water returns, there is a contribution from the asymmetric effect of off-pointing over a wide river. It was seen that the number of potential altimetric heights increased by 66% when incorporating off-nadir water locations, although the additional cross-angle range correction, with its additional error source, did affect the fit to the gauge data, yielding an RMSE of 0.524 m in Run (ii_3).

Residuals plotted as a function of months of the year showed a preponderance of high positive residuals during the dry season, as evidenced in the RMSEs of fit for July–November andJanuary–June and December, inclusive, of 0.536 m and 0.461 m, respectively. The low flow and change in river cross-section in the dry season were problematic in establishing true water reflections, with sub-satellite points falsely identified as water during low flow regimes. It is pertinent that the SRTM mask derived from data in February 2000 corresponds to medium seasonal flow. At Tabatinga, the river is typically of max/min height and discharge in May and September–October, respectively, although the minimum can occur later, as in November 2000. Gauge heights at Tabatinga show a range of 10.6 m in 2000, with a maximum reading of 102 m on 19 May and a minimum of 2.39 m on 24 November. For the SRTM of 11–22 February 2000, during the rising period, the average recording at Tabatinga was 7.82 m, corresponding to a near-average flow. Low-flow regimes are the areas in Figure 6 where the probabilistic extent of the Amazon is above 70% from [34]. Figure 6 shows that the SRTM mask tends to exclude high-flow areas (below 30% probability). During low flow, the altimetry is apparently recording measurements from land close to the river, which appear as strong specular signatures. During the wet season, the returns are as expected, as the conservative SRTM mask identifies the water extent.

A more realistic dynamic mask, or prescribing the probabilistic extent to the seasonal cycle, could lead to an improvement during the dry season. This is a recurrent issue when using a static water mask. A dynamic, seasonal, and multi-year mask will be necessary to counteract this deficiency, such as that derived from contemporary river data from Landsat, for example. Alternatively, an approach could be used, such as that in [35], where topography-aware, regional-scale optimisation improves precipitation fields, which can be used to support dynamic water masks and seasonal weighting.

The gauge-to-altimetric height model solved the river slope and velocity, with the least-squares fit yielding a river slope of -0.03506 ± 0.00003 m/km and a mean velocity of 1.803 ± 0.014 m/s over a river stretch of 285 km. For comparison, Ref. [36] gave a characteristic velocity of 1.69 m/s from the Hybam database for the station at Tamshiyacu,

1605 km upstream of Tabatinga. Ref. [37] gave stream velocities at Tabatinga of 2.12 m/s for high discharge and 1.34 m/s for lower discharge. As a single stream velocity was employed in the altimetric analysis, the derived result will be averaged across multiple years and seasons. The mean of the values [37] is consistent with the characteristic velocity. The altimetrically derived velocity is higher than the characteristic value and will be biased towards the higher discharge regime, as discernible stream wave characteristics will be more marked at high flow. It is likely that at low flows, waves between the altimetric crossing point and Tabatinga will be less pronounced, with the time lapse less well defined.

The altimetric slope values are complementary to slopes derived from the Shuttle Radar Topography Mission digital elevation model [38], with computed slopes of 0.0192 m/km at Manacapuru, sited at 3.29972°S, 60.62056°W on the Amazon, and 0.0320 m/km at Tupe, 3.045614°S, 60.252933°W, on the Negro, 25 km from Manaus. It is noted that, with the SRTM, water surface elevation error can be inferred as 3.9 m for basin-wide, regional, and local Amazon mainstem reaches; a minimum reach of 733 km is required to calculate a reliable SRTM water-surface slope compared to the 285 km altimetric stretch.

Although highly sensitive to the roll angle, the solution for a correction to this angle had little effect due to the accuracy of the GDR roll angle. The inland water results confirm that the roll angle of the Cryosat-2 GDR is essentially correct, as was also established for the oceanic pass. The solution for the sigma nought ratio, $\hat{\sigma}$ of Equation (28) in the range correction model, is less straightforward. The correction is strongly dependent on the cross-angle, and hence, data with the full cross-angle range is necessary for a meaningful solution. However, at the level of accuracy for the Amazon passes, the solution for $\hat{\sigma}$ had a negligible impact, and the theory will need validation with a more accurate dataset. With reference to Figure 8, $\hat{\sigma} = 0.0013$ equates to powers of 4 and 44 for peak powers of 3000 and 30,000, respectively, in the waveforms. Such values are within the noise level outside the specular peak, as required.

Motivated by the availability of SARin data, this study shows the benefit of correcting for cross-track off-pointing. Even for so-called nadir reflection, improvements have been made. Further improvements may require refinement of the altimetric range correction, possibly including a restriction on the range of cross-angles. Any model, such as one derived from a thin-beam approach, has associated error, and it is unlikely that the range correction can ever be exact for large cross-angles. Accordingly, there is a compromise to be made between potential accuracy and the number of data points utilised. For large rivers, such as the Amazon, it is not unrealistic to restrict correction of the (#,1) solutions of Table 1 to a cross-angle within a range of $\pm 0.4°$, but for narrower rivers and lakes, it may be necessary to utilise all off-nadir reflections to provide sufficient water heights for temporal study. Such decisions are target-dependent. Of course, consideration can also be given to more advanced retracking algorithms than OCOG, including multi-peaked and machine learning approaches.

Author Contributions: Conceptualisation, P.M.; methodology, P.M.; software, P.M. and C.P.; validation, P.M. and C.P.; formal analysis, P.M.; data curation, C.P.; writing, P.M.; visualisation, P.M.; project administration, P.M. All authors have read and agreed to the published version of the manuscript.

Funding: This research received no external funding.

Data Availability Statement: No new data were created or analyzed in this study.

Acknowledgments: The authors wish to thank the European Space Agency for Cryosat-2 data and HYMAM (the Amazon basin water resources observation service, https://hybam.obs-mip.fr/ (accessed on 19 March 2020) for the Tabatinga gauge data. The authors also wish to thank Miles Clements for supplying the SRTM mask.

Conflicts of Interest: The authors declare no conflicts of interest.

Abbreviations

The following abbreviations are used in this manuscript:

FBR	Full Bit Rate
FFT	Fast Fourier Transform
GDR	Geophysical Data Record
HPF	High
L1A	Level 1A
LRM	Low Resolution Mode
OGOG	Offset Centre of Gravity
POCA	Point of Closest Approach
RMSE	Root Mean Square Error
SAR	Synthetic Aperture Radar
SARin	Synthetic Aperture Radar Interferometry
SRTM	Shuttle Radar Topography Mission

Appendix A

The altimetric range, l, for a ground point of cross-track angle, θ, is an overestimation, Δ, of the nadir height, N, where, for a spherical Earth of radius R, $\Delta = l - N$. Upon using the cosine rule in Figure A1 with $N = l - \Delta$, it is easy to show that Δ satisfies

$$\Delta^2 - 2\Delta(R + l(1 - cos\theta)) + 2l(l + R)(1 - cos\theta) = 0$$

Solving for Δ gives

$$\Delta = R + l(1 - cos\theta) \pm R\left(1 - \frac{l^2}{R^2} sin^2\theta\right)^{\frac{1}{2}}$$

Taking the negative root for a solution in the adjacent quadrant and expanding for small θ gives

$$\Delta \approx 2lsin^2\frac{\theta}{2} + \frac{l^2}{2R} sin^2\theta. \quad \text{(A1)}$$

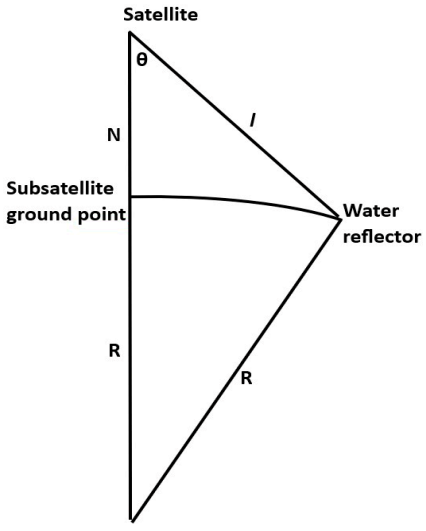

Figure A1. Schematic of the geometry of a satellite of height N above a spherical Earth of radius R. The altimetric range, l, is for a ground point of the cross-track angle, θ.

Appendix B

Consider the Cryosat-2 orbit projected onto a unit sphere (Figure A2), where the sub-satellite point, S, along orbit SS′ has argument of latitude u, geographic latitude φ, and longitude λ; the orbital inclination is i. The water reflector at R is geolocated across-track from S at latitude φ'. Distance SR is the geocentric angle, ζ, with distance SE′ being w. Using spherical trigonometry, the latitude, φ', and longitude, λ', of R are found from

$$sinu = sin\varphi / sini$$

$$w = -tan^{-1}(cosu\ sini)$$

$$cosU = cosu\ sini$$

$$sin\varphi' = sinU\ sin(w - \zeta)$$

$$cos\Delta\lambda = (cos\zeta - sin\varphi\ sin\varphi')/(cos\varphi\ cos\varphi')$$

where $\Delta\lambda$ is the change in longitude, $\lambda - \lambda'$.

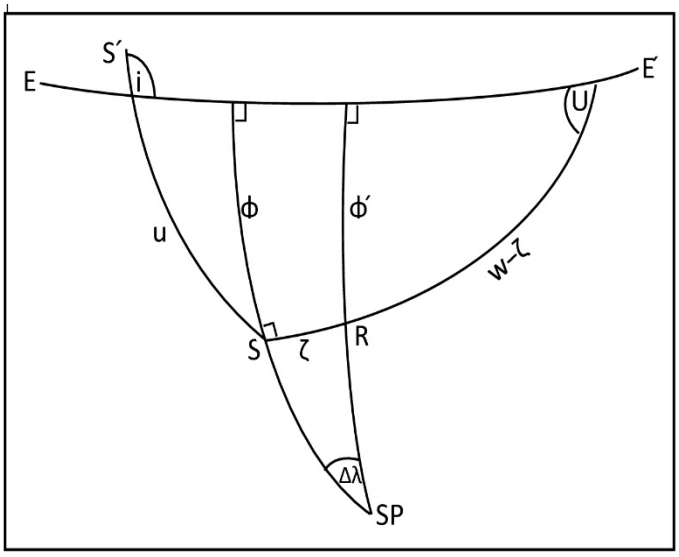

Figure A2. Satellite orbit of inclination, i, projected onto the unit sphere. Satellite at S moving northwards towards S′, equator E E′; SP denotes south pole and R the inland water reflector.

References

1. Birkett, C.M. The contribution of TOPEX/POSEIDON to the global monitoring of climatically sensitive lakes. *J. Geophys. Res. Oceans* **1995**, *100*, 25179–25204. [CrossRef]
2. Berry, P.A.M.; Garlick, J.D.; Freeman, J.A.; Mathers, E.L. Global inland water monitoring from multi-mission altimetry. *Geophys. Res. Lett.* **2005**, *32*, L16401. [CrossRef]
3. Birkinshaw, S.J.; O'Donnell, G.M.; Moore, P.; Kilsby, C.G.; Fowler, H.J.; Berry, P.A.M. Using satellite altimetry data to augment flow estimation techniques on the Mekong River. *Hydrol. Process.* **2010**, *24*, 3811–3825. [CrossRef]
4. Schwatke, C.; Dettmering, D.; Börgens, E.; Bosch, W. Potential of SARAL/AltiKa for inland water applications. *Mar. Geod.* **2015**, *38*, 626–643. [CrossRef]
5. Kittel, C.M.M.; Jiang, L.; Tøttrup, C.; Bauer-Gottwein, P. Sentinel-3 radar altimetry for river monitoring—A catchment-scale evaluation of satellite water surface elevation from Sentinel-3A and Sentinel-3B. *Hydrol. Earth Syst. Sci.* **2021**, *25*, 333–357. [CrossRef]
6. Donlon, C.J.; Cullen, R.; Giulicchi, L.; Vuilleumier, P.; Francis, C.R.; Kuschnerus, M.; Simpson, W.; Bouridah, A.; Caleno, M.; Bertoni, R.; et al. The Copernicus Sentinel-6 mission: Enhanced continuity of satellite sea level measurements from space. *Remote Sens. Environ.* **2021**, *258*, 112395. [CrossRef]
7. Villadsen, H.; Andersen, O.B.; Stenseng, L.; Nielsen, K.; Knudsen, P. CryoSat-2 altimetry for river level monitoring—Evaluation in the Ganges–Brahmaputra River basin. *Remote Sens. Environ.* **2015**, *168*, 80–89. [CrossRef]

8. Schneider, R.; Godiksen, P.N.; Villadsen, H.; Madsen, H.; Bauer-Gottwein, P. Application of CryoSat-2 altimetry data for river analysis and modelling. *Hydrol. Earth Syst. Sci.* **2017**, *21*, 751–764. [CrossRef]
9. Moore, P.; Birkinshaw, S.J.; Ambrózio, A.; Restano, M.; Benveniste, J. CryoSat-2 Full Bit Rate Level 1A processing and validation for inland water applications. *Adv. Space Res.* **2018**, *62*, 1497–1515. [CrossRef]
10. Gao, Q.; Makhoul, E.; Escorihuela, M.J.; Zribi, M.; Seguí, P.Q.; García, P.; Roca, M. Analysis of Retrackers' Performances and Water Level Retrieval over the Ebro River Basin Using Sentinel-3. *Remote Sens.* **2019**, *11*, 718. [CrossRef]
11. Jiang, L.; Nielsen, K.; Andersen, O.B.; Bauer-Gottwein, P. A bigger picture of how the Tibetan lakes have changed over the past decade revealed by CryoSat-2 altimetry. *J. Geophy. Res. Atmos.* **2020**, *125*, e2020JD033161. [CrossRef]
12. Kleinherenbrink, M.; Naeije, M.; Slobbe, C.; Egido, A.; Smith, W. The performance of CryoSat-2 ful-ly-focussed SAR for inland water-level estimation. *Remote Sens. Environ.* **2020**, *237*, 111589. [CrossRef]
13. Roohi, S.; Sneeuw, N.; Benveniste, J.; Dinardo, S.; Issawy, E.; Zhang, G. Evaluation of CryoSat-2 water level derived from different retracking scenarios over selected inland water bodies. *Adv. Space Res.* **2021**, *68*, 947–962. [CrossRef]
14. Kossieris, S.; Tsiakos, V.; Tsimiklis, G.; Amditis, A. Inland Water Level Monitoring from Satellite Observations: A Scoping Review of Current Advances and Future Opportunities. *Remote Sens.* **2024**, *16*, 1181. [CrossRef]
15. Zhang, M.; Lee, H.; Shum, C.K.; Alsdorf, D.; Schwartz, F.; Tseng, K.-H.; Yi, Y.; Kuo, C.-Y.; Tseng, H.-Z.; Braun, A.; et al. Application of retracked satellite altimetry for inland hydrologic studies. *Int. J. Remote Sens.* **2010**, *31*, 3913–3929. [CrossRef]
16. Kuo, C.-Y.; Kao, H.-C. Retracked Jason-2 altimetry over small water bodies: Case study of Bajhang River, Taiwan. *Mar. Geod.* **2011**, *34*, 382–392. [CrossRef]
17. Yang, Y.; Moore, P.; Li, Z.; Li, F. Lake Level Change From Satellite Altimetry Over Seasonally Ice-Covered Lakes in the Mackenzie River Basin. *IEEE Trans. Geosci. Remote Sens.* **2020**, *59*, 8143–8152. [CrossRef]
18. Villadsen, H.; Deng, X.; Andersen, O.B.; Stenseng, L.; Nielsen, K.; Knudsen, P. Improved inland water levels from SAR altimetry using novel empirical and physical retrackers. *J. Hydrol.* **2016**, *537*, 234–247. [CrossRef]
19. Chen, P.; An, Z.; Xue, H.; Yao, Y.; Yang, X.; Wang, R.; Wang, Z. INPPTR: An improved retracking algorithm for inland water levels estimation using Cryosat-2 SARin data. *J. Hydrol.* **2022**, *613*, 128439. [CrossRef]
20. Boergens, E.; Dettmering, D.; Schwatke, C.; Seitz, F. Water level, areal extent and volume change of Lake Tanganyika, Lake Turkana, Lake Tonle Sap and Lake Constance: Multi-year time series from satellite altimetry and remote sensing [dataset publication series]. *PANGAEA* **2017**. [CrossRef]
21. Pearson, C.; Moore, P.; Edwards, S. GNSS assessment of sentinel-3A ECMWF tropospheric delays over inland waters. *Adv. Space Res.* **2020**, *66*, 2827–2843. [CrossRef]
22. Frappart, F.; Calmant, S.; Cauhope, M.; Seyler, F.; Cazenave, A. Preliminary Results of ENVISAT RA-2-Derived Water Levels Validation over the Amazon Basin. *Remote Sens. Environ.* **2006**, *100*, 252–264. [CrossRef]
23. Da Silva, J.S.; Seyler, F.; Calmant, S.; Filho, O.C.R.; Roux, E.; Araújo, A.A.M.; Guyot, J.L. Water level dynamics of Amazon wetlands at the watershed scale by satellite altimetry. *Int. J. Remote Sens.* **2011**, *33*, 3323–3353. [CrossRef]
24. Calmant, S.; Seyler, F.; Cretaux, J.F. Monitoring continental surface waters by satellite altimetry. *Surv. Geophys.* **2008**, *29*, 247–269. [CrossRef]
25. da Silva, J.S.; Calmant, S.; Seyler, F.; Filho, O.C.R.; Cochonneau, G.; Mansur, W.J. Water levels in the Amazon basin derived from the ERS 2 and ENVISAT radar altimetry missions. *Remote Sens. Environ.* **2010**, *114*, 2160–2181. [CrossRef]
26. Maillard, P.; Bercher, N.; Calmant, S. New processing approaches on the retrieval of water levels in EN-VISAT and SARAL radar altimetry over rivers: A case study of the São Francisco River, Brazil. *Remote Sens. Environ.* **2015**, *156*, 226–241. [CrossRef]
27. Frappart, F.; Papa, F.; Marieu, V.; Malbeteau, Y.; Jordy, F.; Calmant, S.; Durand, F.; Bala, S. Preliminary assessment of SARAL/AltiKa observations over the Ganges-Brahmaputra and Irrawaddy Rivers. *Mar. Geod.* **2015**, *38*, 568–580. [CrossRef]
28. Boergens, E.; Dettmering, D.; Schwatke, C.; Seitz, F. Treating the Hooking Effect in Satellite Altimetry Data: A Case Study along the Mekong River and Its Tributaries. *Remote Sens.* **2016**, *8*, 91. [CrossRef]
29. Wingham, D.; Francis, C.; Baker, S.; Bouzinac, C.; Brockley, D.; Cullen, R.; de Chateau-Thierry, P.; Laxon, S.; Mallow, U.; Mavrocordatos, C.; et al. CryoSat: A mission to determine the fluctuations in Earth's land and marine ice fields. *Adv. Space Res.* **2005**, *37*, 841–871. [CrossRef]
30. Kleinherenbrink, M.; Ditmar, P.; Lindenbergh, R. Retracking Cryosat data in the SARIn mode and robust lake level extraction. *Remote Sens. Environ.* **2014**, *152*, 38–50. [CrossRef]
31. Gommenginger, C.; Thibaut, P.; Fenoglio-Marc, L.; Quartly, G.; Deng, X.; Gomez-Enri, J.; Challenor, P.; Gao, Y. Retracking altimeter waveforms near the coasts. A review of retracking methods and some applications to coastal waveforms. In *Coastal Altimetry*; Vignudelli, S., Kostianoy, A.G., Cipollini, P., Benveniste, J., Eds.; Springer: Berlin/Heidelberg, Germany, 2011; pp. 61–101. [CrossRef]
32. Chelton, D.B.; Edward, J.W.; MacArthur, J.L. Pulse Compression and Sea Level Tracking in Satellite Al-timetry. *J. Atmos. Ocean. Technol.* **1989**, *6*, 407–438. [CrossRef]

33. Park, E.; Latrubesse, E.M. Modeling suspended sediment distribution patterns of the Amazon River using MODIS data. *Remote Sens. Environ.* **2014**, *147*, 232–242. [CrossRef]
34. Pekel, J.-F.; Cottam, A.; Gorelick, N.; Belward, A.S. High-resolution mapping of global surface water and its long-term changes. *Nature* **2016**, *540*, 418–422. [CrossRef] [PubMed]
35. Wang, J.; Chen, J.; Shen, P.; Guan, X.; Liu, X.; Massari, C.; Wang, Z.; Feng, M.; Wang, Q.; Lu, Y.; et al. Regional-scale intelligent optimization and topography impact in restoring global precipitation data gaps. *Commun. Earth Environ.* **2025**, *6*, 671. [CrossRef]
36. Chávarri, E.; Crave, A.; Bonnet, M.-P.; Mejía, A.; Da Silva, J.S.; Guyot, J.L. Hydrodynamic modelling of the Amazon River: Factors of uncertainty. *J. S. Am. Earth Sci.* **2013**, *44*, 94–103. [CrossRef]
37. Cruz, J.d.S.; Blanco, C.J.C.; Junior, A.C.P.B. Flow-velocity model for hydrokinetic energy availability assessment in the Amazon. *Acta Sci. Technol.* **2019**, *42*, e45703. [CrossRef]
38. LeFavour, G.; Alsdorf, D. Water slope and discharge in the Amazon River estimated using the shuttle radar topography mission digital elevation model. *Geophys. Res. Lett.* **2005**, *32*. [CrossRef]